

# Chapter 2

## Electrochemical Methods

### 2.1 Chronopotentiometry

In chronopotentiometry, a current pulse is applied to the working electrode and its resulting potential is measured against a reference electrode as a function of time. At the moment when the current is first applied, the measured potential is abruptly changed due to the  $iR$  loss, and after that it gradually changes, because a concentration overpotential is developed as the concentration of the reactant is exhausted at the electrode surface. If the current is larger than the limiting current, the required flux for the current cannot be provided by the diffusion process and, therefore, the electrode potential rapidly rises until it reaches the electrode potential of the next available reaction, and so on.

The different types of chronopotentiometric techniques are depicted in Fig. 2.1. In constant current chronopotentiometry, the constant anodic/cathodic current applied to the electrode causes the electroactive species to be oxidized/reduced at a constant rate. The electrode potential accordingly varies with time as the concentration ratio of reactant to product changes at the electrode surface. This process is sometimes used for titrating the reactant around the electrode, resulting in a potentiometric titration curve. After the concentration of the reactant drops to zero at the electrode surface, the reactant might be insufficiently supplied to the surface to accept all of the electrons being forced by the application of a constant current. The electrode potential will then sharply change to more anodic/cathodic values. The shape of the curve is governed by the reversibility of the electrode reaction.

The applied current can be varied with time, rather than being kept constant. For example, the current can be linearly increased or decreased (chronopotentiometry with linearly rising current in the figure) and can be reversed after some time (current reversal chronopotentiometry in the figure). If the current is suddenly changed from an anodic to cathodic one, the product formed by the anodic reaction (i.e., anodic product) starts to be reduced. Then, the potential moves in the cathodic direction as the concentration of the cathodic product increases. On the other hand, the current is repeatedly reversed in cyclic chronopotentiometry.

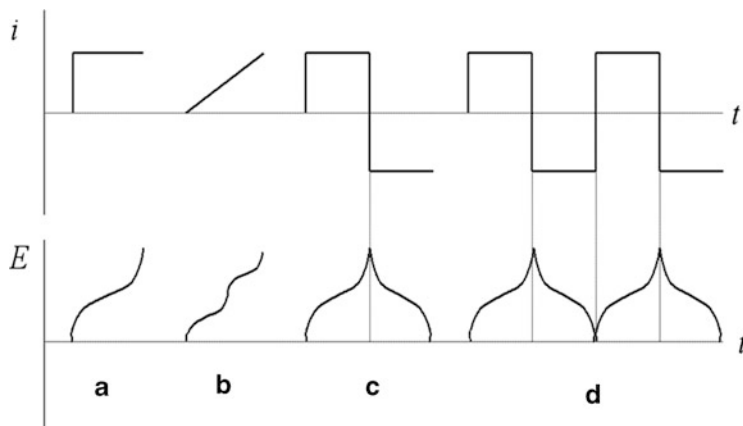
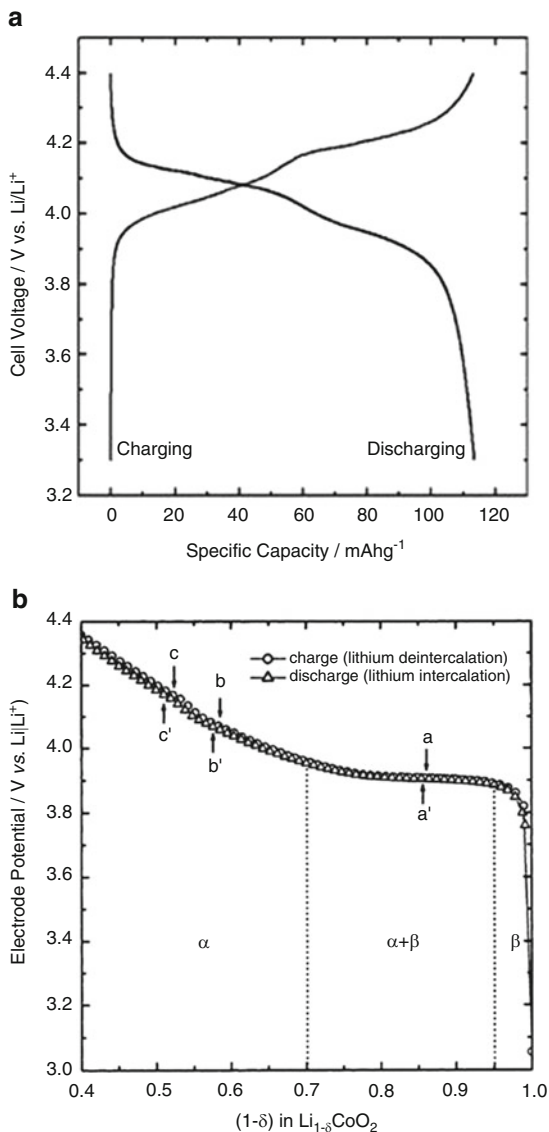


**Fig. 2.1** Different types of chronopotentiometric experiments. (a) Constant current chronopotentiometry. (b) Chronopotentiometry with linearly rising current. (c) Current reversal chronopotentiometry. (d) Cyclic chronopotentiometry

The typical chronopotentiometric techniques can be readily extended to characterize the electrochemical properties of insertion materials. In particular, current reversal and cyclic chronopotentiometries are frequently used to estimate the specific capacity and to evaluate the cycling stability of the battery, respectively. Shown in Fig. 2.2a is a typical galvanostatic charge/discharge profile of  $\text{LiMn}_2\text{O}_4$  powders at a rate of 0.2 C (In battery field,  $n\text{C}$  rate means the discharging/charging rate at which the battery is virtually fully discharged/charged for  $1/n$  h.) [1]. The total quantity of electricity per mass available from a fully charged cell (or storable in a fully discharged cell) can be calculated at a specific C rate from the charge transferred during the discharging (or charging) process in terms of  $\text{C}\cdot\text{g}^{-1}$  or  $\text{mAh}\cdot\text{g}^{-1}$ . Alternatively, the quantity of electricity can be converted to the number of moles of inserted atoms as long as the electrode potential is obtained in a (quasi-) equilibrium state (Fig. 2.2b [2]; for more details, please see the explanation below on the galvanostatic intermittent titration technique). The specific capacity is frequently measured at different discharging rates to evaluate the rate capability of the cell (Fig. 2.3) [3].

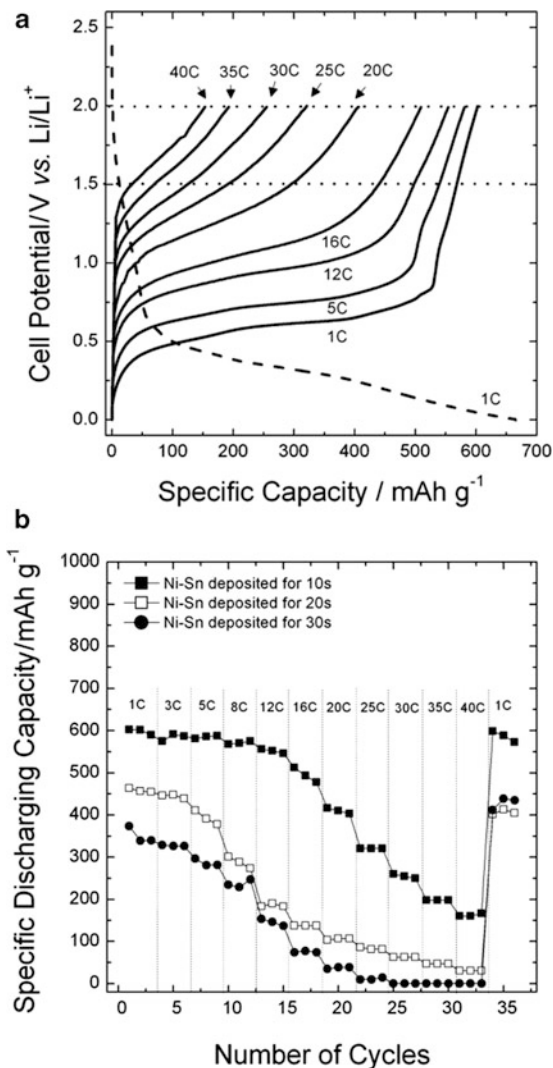
The voltage profile, obtained by current reversal or cyclic chronopotentiometry, can be effectively used to characterize the multi-step redox reactions during the insertion process. An example is given in Fig. 2.4 for  $\text{Cu}_6\text{Sn}_5$  which is one of the anodic materials that can be used in rechargeable lithium batteries [4]. The differential capacity curve  $dC/dE$  (Fig. 2.4b), which is reproduced from the voltage versus specific capacity curve of Fig. 2.4a, clearly shows two reduction peaks and the corresponding oxidation peaks. The reduction peaks, R1 and R2, are caused by the phase transformation of  $\text{Cu}_6\text{Sn}_5\text{-Li}_2\text{CuSn}$  and the subsequent formation of  $\text{Li}_{4.4}\text{Sn}$ , while the oxidation peaks, O1 and O2, are ascribed to the corresponding reverse reactions for the formation of  $\text{Li}_2\text{CuSn}$  and  $\text{Cu}_6\text{Sn}_5$ , respectively [5, 6].

**Fig. 2.2** (a) Galvanostatic charge/discharge curve of  $\text{LiMn}_2\text{O}_4$  and (b) open-circuit potential versus lithium stoichiometry plot of  $\text{LiCoO}_2$  (Reprinted from Zhang et al. [1], Copyright ©2004, and Shin and Pyun [2], Copyright ©2001, with permissions from Elsevier Science)



The galvanostatic intermittent titration technique (GITT) is considered to be one of the most useful techniques in chronopotentiometry. In the GITT, a constant current is applied for a given time to obtain a specific charge increment and then it is interrupted to achieve open circuit condition until the potential change is virtually zero. This process is repeated until the electrode potential reaches the cut-off voltage. Eventually, the equilibrium electrode potential is obtained as a function of lithium content, as shown in Fig. 2.5 [7]. Another important usage of the GITT is

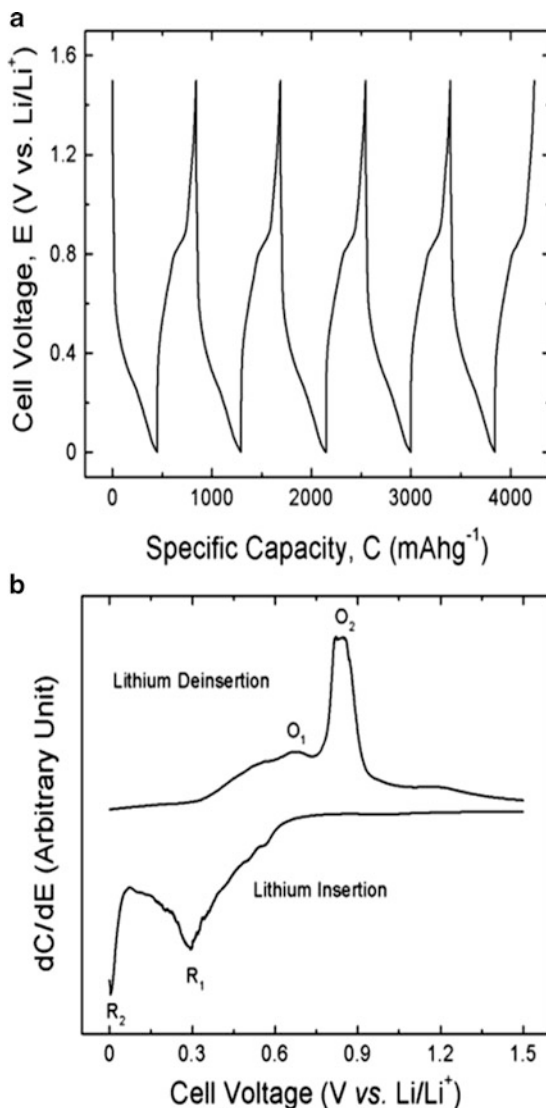
**Fig. 2.3** (a) Voltage profiles of the electrodeposited Ni-Sn foam with nanostructured walls at different discharging (lithium dealloying) rates, and (b) dependence of specific capacity on discharging rate, obtained from the samples created at different deposition times (Reprinted from Jung et al. [3], Copyright ©2011 with permission from Elsevier Science)



the estimation of the chemical diffusion coefficient of the species in the insertion materials [8–10]. When the diffusion process in the material is assumed to obey Fick's diffusion equations for a planar electrode, the chemical diffusion coefficient can be expressed as follows [8]:

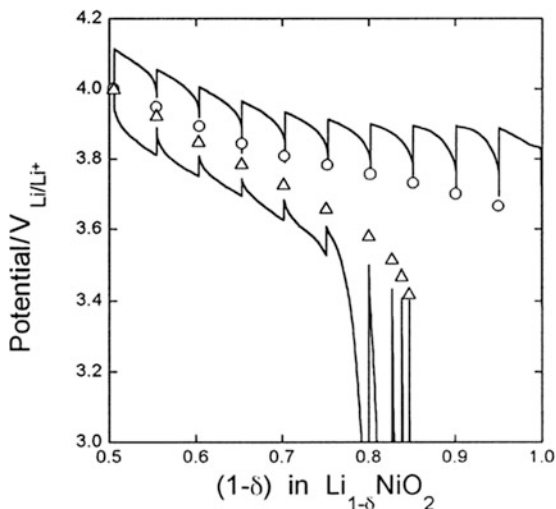
$$\tilde{D} = \frac{4}{\pi} \left( \frac{I_0 V_m}{z_i F S} \right)^2 \left[ \left( \frac{dE}{d\delta} \right) / \left( \frac{dE}{d\sqrt{t}} \right) \right]^2 \text{ for } t \ll \frac{l^2}{\tilde{D}} \quad (2.1)$$

**Fig. 2.4** (a) Galvanostatic charge/discharge curves of the electrodeposited  $\text{Cu}_6\text{Sn}_5$  porous film, and (b) the differential capacity  $dC/dE$  versus cell voltage plot, determined from (a) (Reprinted from Shin and Liu [4], Copyright ©2005 with permission from WILEY-VCH Verlag GmbH & Co)



where  $V_m$  is the molar volume of the active material;  $z_i$ , the valence number of diffusing species;  $F$ , the Faraday constant;  $S$ , the surface area of the material;  $I_0$ , the applied constant current;  $(dE/d\delta)$ , the dependence of electrode potential on the stoichiometry of the inserted atoms;  $(dE/d\sqrt{t})$ , the dependence of the electrode potential on the square root of time; and  $l$ , the thickness of the electrode (or solid state-diffusion length).

**Fig. 2.5** Typical galvanostatic intermittent charge–discharge curves of the  $\text{Li}_{1-\delta}\text{NiO}_2$  composite electrode (Reprinted from Choi et al. [7], Copyright © 1998 with permission from Elsevier Science)



## 2.2 Chronoamperometry

The current transient technique is another name for chronoamperometry. In this technique, the electrode potential is abruptly changed from  $E_1$  (the electrode is usually in the equilibrium state at this potential) to  $E_2$  and the resulting current variation is recorded as a function of time. The interpretation of the results is typically based on a planar electrode in a stagnant solution and an extremely fast interfacial redox reaction as compared to mass transfer. Figure 2.6 shows the potential stepping in chronoamperometry, the resulting current variation with time, and the expected content profile of the active species in the electrolyte.

Chronoamperometry has been widely used to characterize the kinetic behavior of insertion materials. The typical assumption for the analysis of the chronoamperometric curve (or current transient) of insertion materials is that the diffusion of the active species governs the rate of the whole insertion process. This means the following: The interfacial charge-transfer reaction is so kinetically fast that the equilibrium concentration of the active species is quickly reached at the electrode surface at the moment of potential stepping. The instantaneous depletion (or accumulation) of the concentration of active species at the surface caused by the chemical diffusion away from the surface to the bulk electrode (or to the interface away from the bulk electrode) is completely compensated by the supply from the electrolyte (or release into the electrolyte). This is referred to hereafter as the *potentiostatic* boundary condition. The interface between the electrode and current collector is typically under the *impermeable* boundary condition where the atom cannot penetrate into the back of the electrode. Conceptual illustrations of the *potentiostatic* and *impermeable* boundary conditions are presented in Fig. 2.7 along with their mathematical expressions.

**Fig. 2.6** (a) Schematic illustration of the potential stepping in chronoamperometry, (b) the resulting current variation with time, and (c) the expected content profile of the active species O in the electrolyte. Bulk concentration of the species O is  $c_o^*$ . Species O is electrochemically inactive at  $E_1$ , but is reduced at  $E_2$

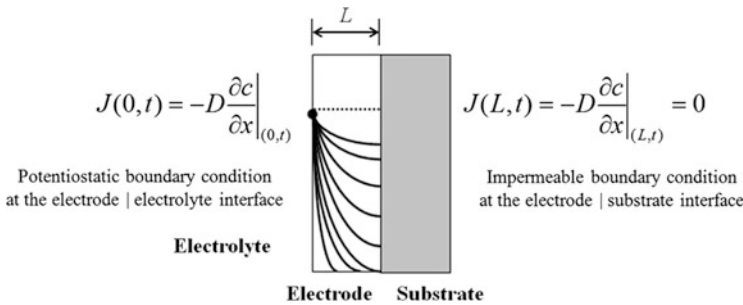
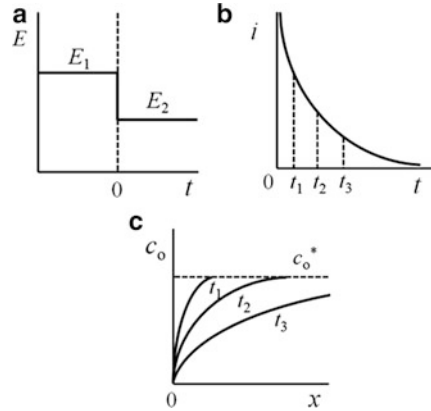


**Fig. 2.7** Schematic illustration of concentration profile of the active species inserted into the electrode under the *potentiostatic* (at the electrode/electrolyte interface) and *impermeable* (at the electrode/substrate interface) boundary conditions, together with the mathematical expressions of the boundary conditions

When the atomic content is constant throughout the electrode before the application of the potential step, and the electrolyte/electrode and electrode/current collector interfaces are under *potentiostatic* and *impermeable* constraints, respectively, the normalized atomic content can be expressed as follows [11–13]:

$$\frac{c(x, t) - c_0}{c_s - c_0} = \sum_{n=0}^{\infty} \left[ (-1)^n \left( \operatorname{erfc} \frac{(n+1)l - x}{\sqrt{Dt}} + \operatorname{erfc} \frac{nl + x}{\sqrt{Dt}} \right) \right]$$

for  $t \ll \frac{l^2}{D}$  (2.2)

$$\frac{c(x, t) - c_0}{c_s - c_0} = -\frac{4}{\pi} \sum_{n=0}^{\infty} \left[ \frac{1}{2n+1} \sin \frac{(2n+1)\pi x}{2l} \exp \left( -\frac{(2n+1)^2 \pi^2 \tilde{D} t}{4l^2} \right) \right]$$

for  $t \gg \frac{l^2}{\tilde{D}}$

(2.3)

Equations 2.2 and 2.3 are useful to predict the atomic content in the electrode at the initial and later stages of the diffusion process, respectively. From the definition of the current given by

$$I(t) = -z_i F S \tilde{D} \left( \frac{\partial c(x, t)}{\partial x} \right)_{x=0}$$
(2.4)

Equations 2.2 and 2.3 become

$$I(t) = \frac{Q}{l} \left( \frac{\tilde{D}}{\pi} \right)^{1/2} t^{-1/2} \quad \text{for } t \ll \frac{l^2}{\tilde{D}}$$
(2.5)

$$I(t) = \frac{2Q\tilde{D}^{1/2}}{l^2} \exp \left( -\frac{\pi^2 \tilde{D}}{4l^2} t \right) \quad \text{for } t \gg \frac{l^2}{\tilde{D}}$$
(2.6)

where  $Q$  is the charge allocated to the atomic insertion/desertion process from  $t = 0$  to  $t \rightarrow \infty$ .

Hence, the current transient shows a linear relation between the logarithmic current and logarithmic time with a slope of  $-0.5$  in the initial stage of diffusion (Eq. 2.5), while it exhibits an exponential decay in the later stage (Eq. 2.6). In other words, the current transient shows a transition from semi-infinite diffusion behavior to finite-length diffusion behavior. The former is called Cottrell behavior.

Presented in Fig. 2.8a–c is the hypothetical open circuit potential curve with the potential drops chosen for the calculation, the resulting theoretically calculated current transients, and the time-dependent content profile across the electrode, respectively [14]. The Cottrell region and the transition time from semi-infinite diffusion to finite-length diffusion are explicitly indicated in figure (b). The content profile of figure (c) helps one understand the diffusion process during the chronoamperometric experiment: At the moment of potential stepping ( $t = 0$ ), a new equilibrium content of the active species is imposed on the electrode surface. Then, the species diffuses into the electrode due to the content gradient. The resulting depletion of the species at the electrode surface is compensated by the continuous supply of the species from the electrolytic phase (although this process is not explicitly illustrated in the figure) and, as a result, the surface content of the species remains constant. As the diffusion time goes on, the content of the species in the electrode approaches the equilibrium composition of the final potential everywhere.

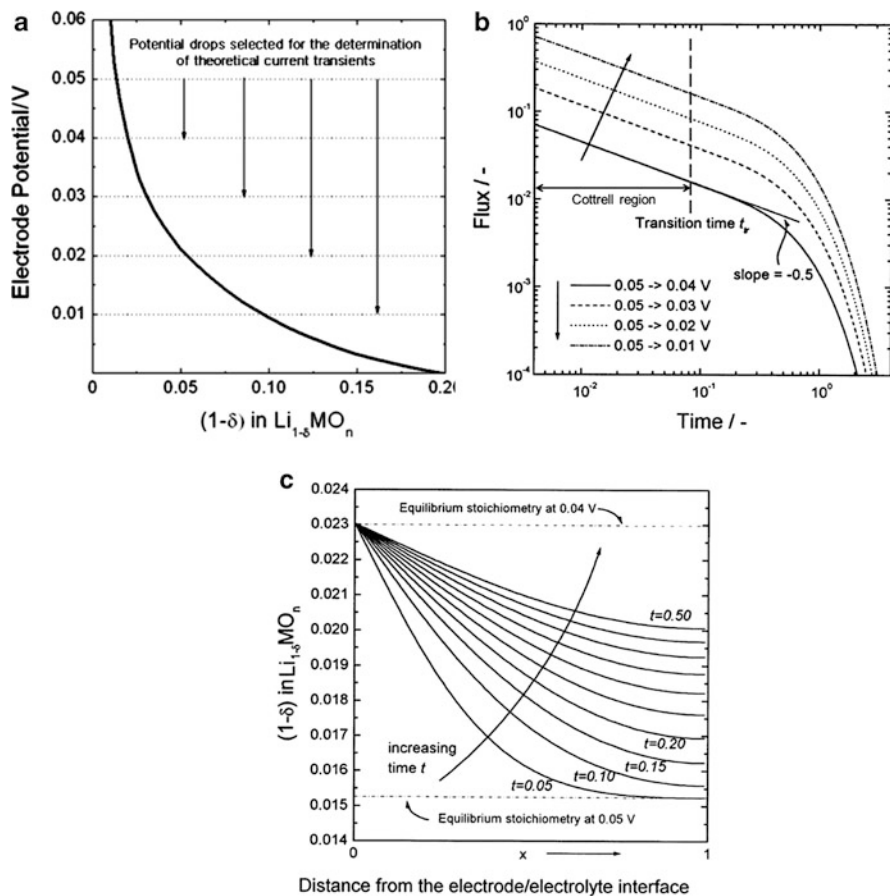
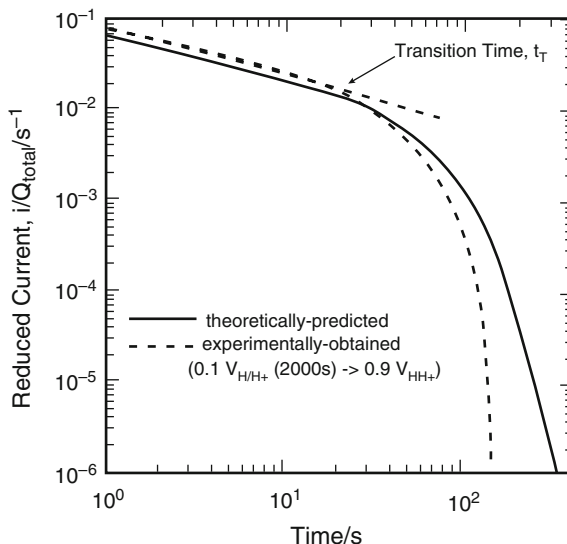


**Fig. 2.8** (a) Hypothetic electrode potential curve, (b) the cathodic current transients at the potential drops of 0.05 V to different lithium insertion potentials, and (c) the change in lithium content profile across the electrode with time at the potential drop of 0.05–0.04 V. The *potentiostatic* and *impermeable* boundary conditions are assumed for the calculation (Reprinted from Shin and Pyun [14], Copyright ©1999 with permission from Elsevier Science)

The current transient for the insertion electrode can be classified into the following two types: The current buildup transient for the cathodic potential step and the current decay transient for the anodic potential step. It is expected that the active species is inserted into the electrode in the former, while it is extracted from the electrode in the latter. However, the current build-up transient occasionally includes the information of other (side) reaction than just the insertion of the active species. For example, when insertion materials such as Pd and  $\text{LaNi}_5$  combine with hydrogen and form metal hydrides, hydrogen insertion (or hydride-forming process) accompanies sometimes the hydrogen evolution reaction. Accordingly, the current transient includes the information of both hydrogen insertion into the electrode and hydrogen evolution at the interface. Under the circumstances, the time-dependent hydrogen content in the electrode cannot be properly estimated

**Fig. 2.9** Reduced current decay transients of PdH<sub>x</sub> electrode when the potential is jumped from 0.1 to 0.90 V<sub>H/H+</sub>. Before potential jump, the hydrogen was injected to the Pd at 0.1 V<sub>H/H+</sub> for 2,000 s (Reprinted from Shin et al. [15], Copyright ©1998 with permission from Corrosion Science Society of Korea)



from the current transient. Consequently, in the case of a metal hydride electrode, Eqs. 2.5 and 2.6 are valid only for the current build-up transient obtained in the hydrogen-evolution-free region and current decay transient (Fig. 2.9) [15].

A number of current transients have been analyzed on the basis of Eqs. 2.5 and 2.6. Particularly, the slopes of  $I(t)$  versus  $t^{-1/2}$  (or the values of  $I(t) \cdot t^{1/2}$ ) and  $\ln I(t)$  versus  $t$  curves have been determined in the initial and later stages of the diffusion process of the active species, respectively, to estimate its chemical diffusion coefficient in the electrode. However, it has been reported that the chemical diffusion coefficient determined from the current transient technique on the basis of the *diffusion control* process shows a large discrepancy from those values determined by other electrochemical techniques such as the GITT and electrochemical impedance spectroscopy (EIS) [16–19]. Furthermore, a number of anomalous shapes observed in current transients, which were never explained on the grounds of the *diffusion-controlled process*, have been reported for different insertion materials [20–23]. Several attempts have been made to explain these atypical behaviors of the current transient using modified *diffusion-controlled* concepts or completely new concepts. These considered the trapping/detrapping of the diffusing species [24], strain-induced diffusion [25], geometrical effect of the electrode surface [26, 27], phase transformation [28, 29], and internal cell-impedance [14, 30, 31].

## 2.3 Voltammetry

Voltammetry is basically referred to as techniques with the common characteristics that the potential of the working electrode is controlled and the resulting current flow is measured. One of the most general applications is “linear-sweep voltammetry

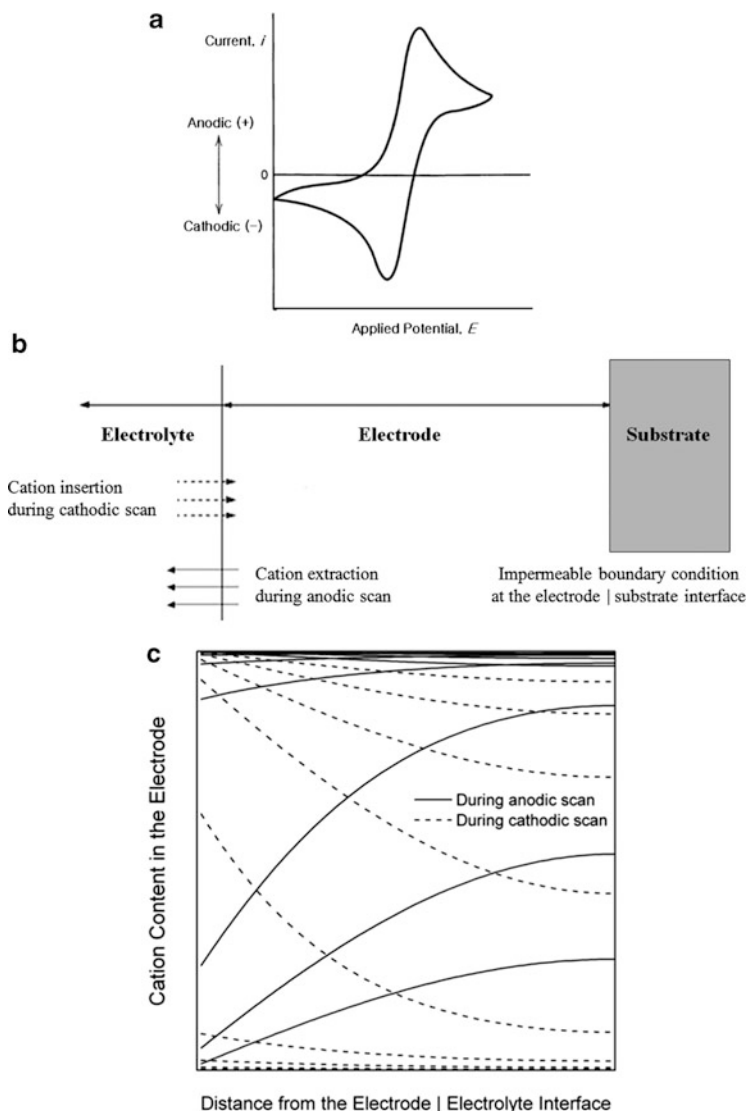
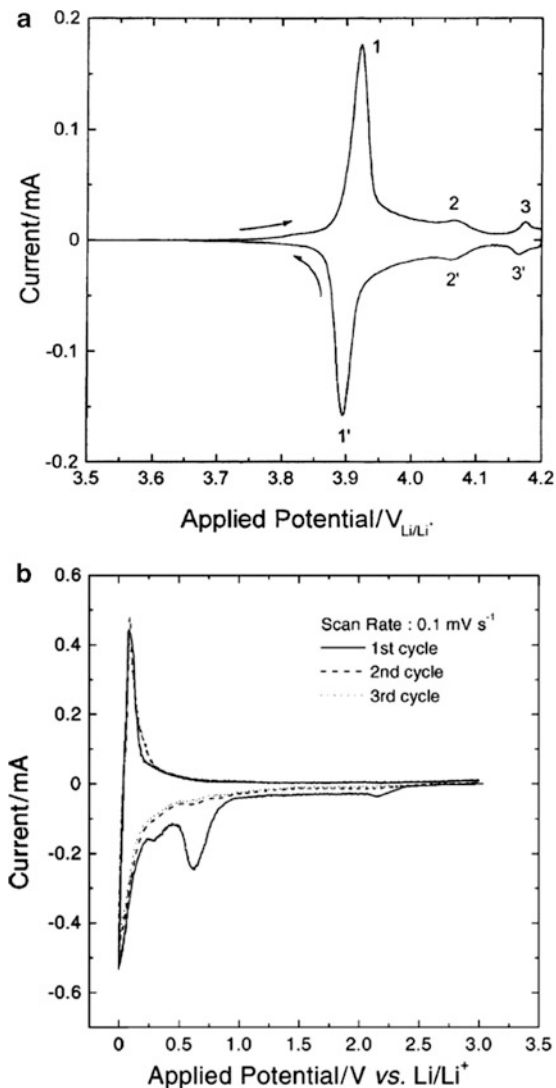


**Fig. 2.10** (a) Typical shape of cyclic voltammogram, (b) the cation movement during potential scan, and (c) the expected potential (or time) dependence of the cation content profile

(LSV or LV)” where the potential is linearly scanned over time in either the negative or positive direction. “Cyclic voltammetry (CV)” is a set of LSV experiments in which anodic and cathodic scans are repeated alternately. That is, at the end of the first scan of LSV, the scan is continued in the reverse direction. This cycle can be repeated a number of times. Schematically shown in Fig. 2.10a–c are typical cyclic voltammogram, the cation movements during potential scans, and the expected voltage (or time) dependence of the cation content profile, respectively.

**Fig. 2.11** The cyclic voltammograms of (a) a sputter-deposited  $\text{LiCoO}_2$  film electrode and (b) multi-walled carbon nanotubes (MWNTs), tested as a cathode and an anode, respectively, in a rechargeable lithium battery (Reprinted from Shin and Pyun [2], Copyright ©2001 and Shin et al. [32], Copyright ©2002, with permissions from Elsevier Science)



The voltammogram gives us information on the possible redox reactions of the system, including the Faradaic insertion and extraction reaction. Figure 2.11a presents the cyclic voltammogram of an  $\text{LiCoO}_2$  film electrode as a cathode in rechargeable lithium battery [2]. Three sets of anodic/cathodic current peaks are observed. The first set of anodic/cathodic current peaks showing the largest value is caused by the insertion/extraction-induced phase transformation from/to Li-diluted hexagonal phase to/from Li-concentrated hexagonal phase. The second and third sets are due to the insertion (extraction)-induced order–disorder phase transition.

Furthermore, the presence of a surface reaction and its reversibility during the atom insertion-extraction process can be successfully examined using voltammetry. Shown in Fig. 2.11b is the cyclic voltammograms for the first three cycles obtained from multi-walled carbon nanotubes (MWNTs) tested as an anode in a rechargeable lithium battery [32]. Aside from the reversible high-current redox signals below 0.5 V versus Li/Li<sup>+</sup>, originating from the lithium insertion/extraction process, there are three irreversible peaks in the first cathodic scan. The two peaks below 1.0 V versus Li/Li<sup>+</sup> are caused by the formation of a solid electrolyte interphase (SEI) layer on the surface of the MWNT electrode, while the peak above 2.0 V versus Li/Li<sup>+</sup> is possibly due to the reduction of the oxygenated species.

Similar to chronoamperometry, the diffusion-controlled model has been usually used to analyze the voltammetric response of the insertion electrode. When an electrode initially holds at a potential  $E_i$ , where the electrode is in the equilibrium state, the linear or cyclic potential scanning is expressed at a scan rate  $\nu$  (V/s) as  $E(t) = E_i \pm \nu t$ . With the assumption of diffusion-controlled atomic transport, the flux balance based on Fick's law and the Nernst equation for voltammetry can be obtained in the same manner as the traditional equations for the combined process of liquid phase diffusion and the interfacial redox reaction. Nevertheless, the inability to use the Laplace transform procedure to figure out the equations greatly complicates the mathematics and makes it quite difficult to get a generalized expression for the potential-dependent current response during the voltammetric experiment.

The analytical solution of the peak current  $I_p$  on the assumption of the semi-infinite diffusion condition is known as the Sevcik equation and expressed as follows [33],

$$I_p = 2.69 \times 10^5 z_i^{3/2} S \tilde{D}^{1/2} \nu^{1/2} c_0 \quad (2.7)$$

In the case of finite-space diffusion, the reversible accumulation/consumption reaction can be characterized by the peak current.

$$I_p = \frac{z_i^2 F^2 \nu l S c_0}{2RT} \quad (2.8)$$

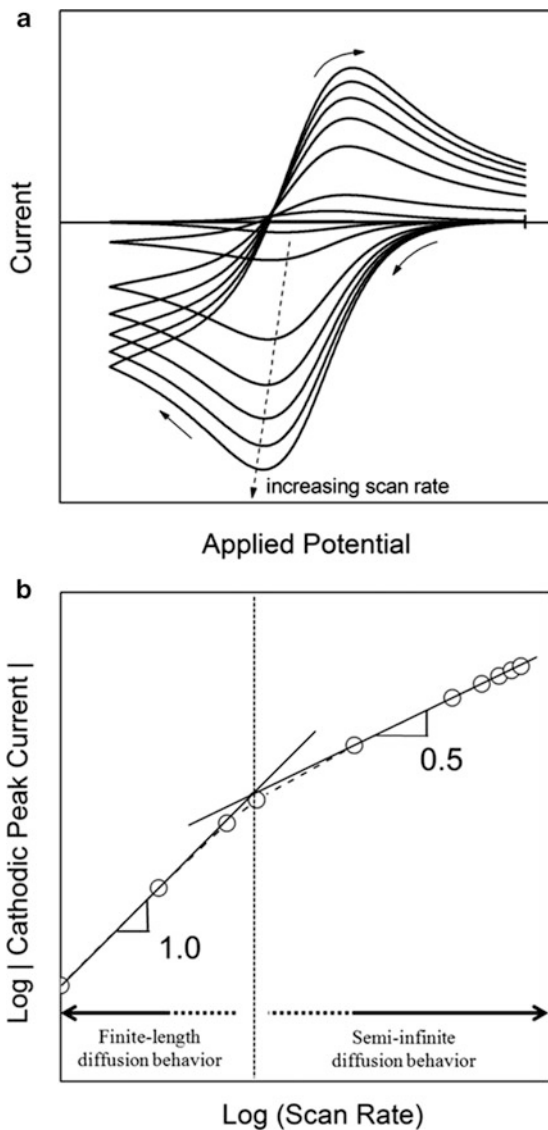
Equation 2.7 indicates that the diffusion coefficient can be estimated from the intercept of the  $\ln I_p$  versus  $\nu$  plot.

The approximate analytical solution for the generalized case has been derived by Aoki *et al.* for the dependence of the peak current, peak potential and half-peak width on the thickness of the electrode and the potential scan rate, in the whole range of scan rates. In particular, the relationship between the peak current and scan rate is given by [34]

$$I_p = 0.446 z_i F S (\tilde{D}/l) c_0 \beta^{0.5} \tanh(0.56 \beta^{0.5} + 0.05 \beta) \quad (2.9)$$

where  $\beta (= z_i F \nu (l^2/D)/RT)$  is a dimensionless characteristic time parameter.

**Fig. 2.12** (a) The cyclic voltammograms at different scan rates and (b) the plot of cathodic peak current density versus scan rate, reproduced from (a)



Presented in Fig. 2.12a are the cyclic voltammograms expected at different scan rates. Two regions of finite-length diffusion and semi-infinite diffusion are indicated at low- and high-rate potential scanning, respectively, in the reproduced plot for the variation of the peak current with the scan rate (Fig. 2.12b).

## 2.4 Electrochemical Impedance Spectroscopy

In electrochemical impedance spectroscopy (EIS), the system under investigation (typically in the equilibrium state) is excited by a small amplitude ac sinusoidal signal of potential or current in a wide range of frequencies and the response of the current or voltage is measured. Since the amplitude of the excitation signal is small enough for the system to be in the (quasi-)equilibrium state, EIS measurements can be used to effectively evaluate the system properties without significantly disturbing them. Frequency sweeping in a wide range from high-to low-frequency enables the reaction steps with different rate constants, such as mass transport, charge transfer, and chemical reaction, to be separated.

For typical impedance measurements, a small excitation signal (e.g.,  $<20 \sim 30$  mV<sub>rms</sub>) is used, so that the cell is considered as a (pseudo-)linear system. In this condition, a sinusoidal potential input to the system leads to a sinusoidal current output at the same frequency. As a matter of fact, the output current exponentially increases with the applied potential (or polarization, over-voltage), that is, the typical electrochemical system is not linear. When we take a closer look at a very small part of a current versus voltage curve, however, the relation might be regarded as (pseudo-)linear. If we use an excitation signal with a large amplitude and, in doing so, the system is deviated from linearity, the current output to the sinusoidal potential input contains the harmonics of the input frequency. Sometimes, the harmonic response is analyzed to estimate the non-linearity of the system, by intentionally applying an excitation potential with a large amplitude.

The system excitation caused by the time-dependent potential fluctuation has the form of

$$E(t) = E_0 \cos(\omega t) \quad (2.10)$$

where  $E(t)$  is the applied potential at time  $t$ ,  $E_0$  is the potential amplitude, and  $\omega$  is the angular frequency that is defined as the number of vibrations per unit time (frequency, Hz) multiplied by  $2\pi$  and expressed in rad/s. In a linear system, the output current signal  $I(t)$  has amplitude  $I_0$  and is shifted in phase by  $\phi$ .

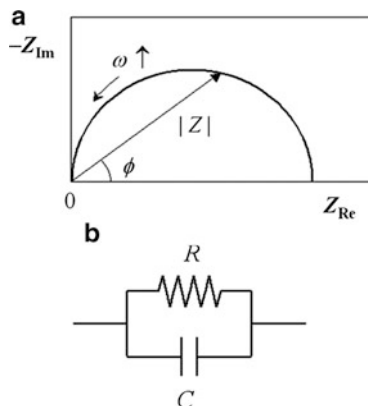
$$I(t) = I_0 \cos(\omega t - \phi) \quad (2.11)$$

Then, the impedance of the system  $Z(t)$  is calculated from Ohm's law:

$$Z(t) = E(t)/I(t) = Z_0 \cos(\omega t)/\cos(\omega t - \phi) \quad (2.12)$$

When we plot the applied potential fluctuation  $E(t)$  on the axis of the abscissa and the resulting current output  $I(t)$  on the axis of the ordinate, we get an oval shape known as a "Lissajous figure" that can be displayed on an oscilloscope screen. By using Euler's relationship defined as  $\exp(j\phi) = \cos\phi + j\sin\phi$ , the system impedance is expressed as a complex function and a lot of useful information on it can be

**Fig. 2.13** (a) Nyquist plot, representing absolute value of impedance vector ( $|Z|$ ), phase angle ( $\phi$ ), and angular frequency ( $\omega$ ) dependence of the impedance, and (b) the corresponding equivalent circuit with  $RC$  parallel element



visualized in quite a simple manner. The excitation potential input and the resulting current output are described as

$$E(t) = E_0 \exp(j\omega t) \quad (2.13)$$

$$I(t) = I_0 \exp[j(\omega t - \phi)] \quad (2.14)$$

Based on Ohm's law, we get the expression for the impedance as a complex number,

$$Z(\omega) = Z_0 \exp(j\phi) = Z_0(\cos \phi + j \sin \phi) \quad (2.15)$$

When the real part of the impedance is plotted on the axis of the abscissa and the imaginary part is plotted on the axis of the ordinate, we get a "Nyquist plot." The example presented in Fig. 2.13a is a graphical expression of the complex plane of the electrical equivalent circuit of Fig. 2.13b. In the Nyquist plot, a vector of length  $|Z|$  is the impedance and the angle between this vector and the real axis is a phase shift,  $\phi$ .

In spite of the wide use of the Nyquist plot, it has a weakness that we cannot know the frequency at which a specific impedance point is recorded in the plot. The "Bode plot" might be useful, in that the frequency information is explicitly shown. In the "Bode plot," the axis of the abscissa is the logarithmic frequency ( $\log \omega$ ) and the axis of the ordinate is either the absolute value of the logarithmic impedance ( $\log |Z|$ ) or phase shift ( $\phi$ ). The Bode plot for the equivalent circuit of Fig. 2.13b is shown in Fig. 2.14.

The Randles circuit is the simplest and most common electrical representation of an electrochemical cell. It includes a resistor (with a resistance of  $R_{ct}$ ; an interfacial charge-transfer resistance) connected in parallel with a capacitor (with a capacitance of  $C_{dl}$ ; a double layer-capacitance) and this  $RC$  electrical unit is connected in series with another resistor (with a resistance of  $R_s$ ; a solution resistance), as shown in Fig. 2.15a. The total impedance of the Randles cell is then expressed by

**Fig. 2.14** Bode plots for the equivalent circuit with  $RC$  parallel element (Fig. 2.13b)

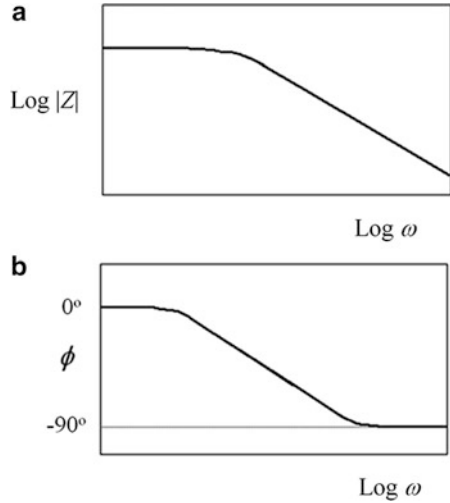
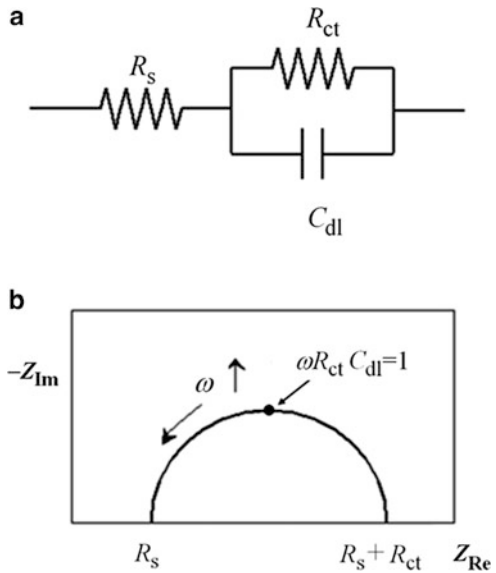


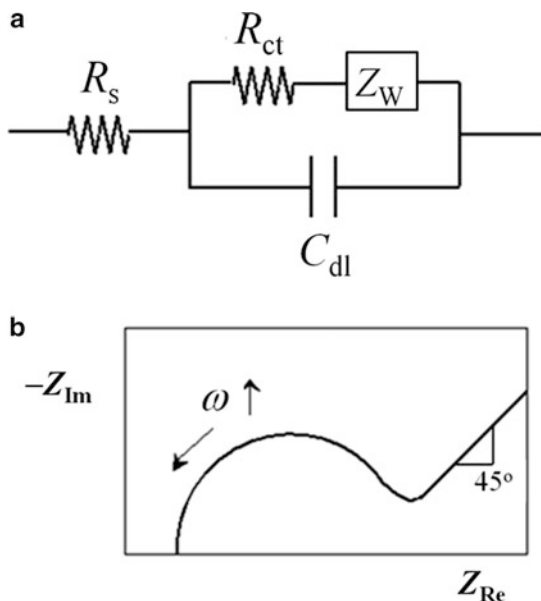
**Fig. 2.15** (a) Randles circuit and (b) its Nyquist plot



$$Z = R_s + (R_{ct}^{-1} + j\omega C_{dl})^{-1} \tag{2.16}$$

From this equation, the real part  $Z_{Re}(= R_s + R_{ct}/(1 + \omega^2 C_{dl}^2 R_{ct}^2))$  and imaginary part  $Z_{Im}(= \omega C_{dl} R_{ct}^2/(1 + \omega^2 C_{dl}^2 R_{ct}^2))$  of the total impedance  $Z(= Z_{Re} + jZ_{Im})$  can be separated. By eliminating the angular frequency,  $\omega$ , we can get the following equation.

**Fig. 2.16** (a) Equivalent circuit including the Warburg element and (b) the typical shape of its Nyquist plot



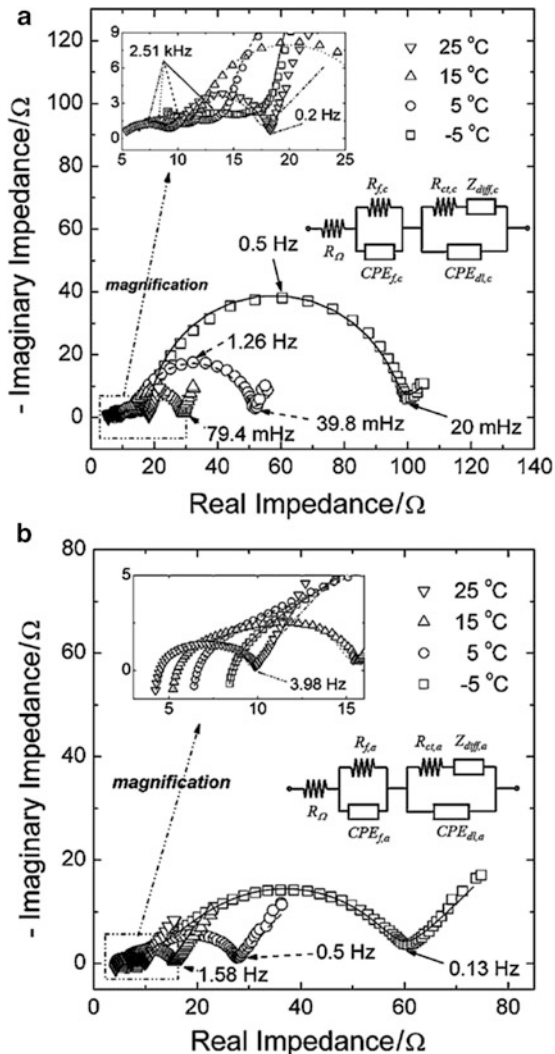
$$Z = \left[ Z_{\text{Re}} - \left( R_s + \frac{R_{\text{ct}}}{2} \right) \right]^2 + R_{\text{Im}}^2 = \left( \frac{R_{\text{ct}}}{2} \right)^2 \quad (2.17)$$

This indicates that the Nyquist plot for a Randles cell is a semicircle with two intercepts on the real axis in the high- and low-frequency regions (Fig. 2.15b). The former is the solution resistance, while the latter is the sum of the solution and charge-transfer resistances. The diameter of the semicircle is therefore equal to the charge-transfer resistance. In addition, the angular frequency is equal to the reciprocal of  $R_{\text{ct}}C_{\text{dl}}$  at the minimum value of  $Z_{\text{Im}}$ .

It should be mentioned that the capacitor (e.g., the double-layer capacitor in the Randles cell) in an impedance experiment frequently does not show ideal behavior. Instead, it acts like an electrical element with constant phase called a constant phase element (CPE) and its impedance has the form of  $Z = A(j\omega)^{-\alpha}$  ( $0.5 < \alpha \leq 1$ ). A few theories have been proposed to explain the deviation of the capacitive behavior from ideality, including the surface roughness effect, but there is no general consensus on the origin of the CPE.

The equivalent circuit of insertion materials includes the diffusion impedance, originating from the solid-state diffusion of the active species. Assuming a semi-infinite diffusion process, the Warburg element with an impedance of  $Z_{\text{w}}$  is connected in series with the resistor representing the interfacial charge transfer,  $R_{\text{ct}}$ , as shown in Fig. 2.16a. The Nyquist plot for the equivalent circuit features an inclined line with a slope of  $45^\circ$  in the low-frequency region, due to the Warburg impedance (Fig. 2.16b).

**Fig. 2.17** Impedance spectra of (a) the  $\text{Li}_{1-x}\text{CoO}_2$  and (b) the graphite at a cell potential of 3.95 V (versus graphite) and different temperatures. The *solid* and *dotted* lines were determined from the CNLS fittings of the impedance spectra to the equivalent circuits presented in the insets. (Reprinted from Cho et al. [36], with permission from Elsevier Science)



When an atom diffuses into the homogeneous single phase, the Warburg impedance  $Z_w$  is expressed as

$$Z_w = \frac{C}{\sqrt{j\omega}} = \frac{C}{\sqrt{2}} \omega^{-1/2} (1 - j) \quad (2.18)$$

where  $C/\sqrt{2}$  is a constant and is called the Warburg coefficient,  $\sigma_w$ . The Warburg coefficient has strong dependence on the chemical diffusion coefficient [35].

$$\sigma_w = \left[ \frac{V_m}{F} \left( \frac{\partial E}{\partial \delta} \right) \frac{1}{\sqrt{2D}} \right] \frac{1}{S} \quad (2.19)$$

The real situation for the insertion process might be more complicated. Shown in Fig. 2.17a, b are the typical impedance spectra of the  $\text{Li}_{1-\delta}\text{CoO}_2$  cathode and graphite anode, respectively, for a rechargeable lithium battery [36]. The first and second semicircles are attributed to the presence of the solid electrolyte interphase (or the particle-to-particle contact of the active materials) and charge-transfer resistance combined with double-layer charging/discharging, respectively [37, 38], while the inclined line (i.e., Warburg element) is due to solid-state lithium diffusion through the active materials.

The measured impedance spectra can be modeled in the simplified phenomenological equivalent circuit shown in the inset of the figure, although different circuit forms might be used according to the physical model employed to interpret the insertion process. The values of the resistance, capacitance, and the chemical diffusion coefficient of lithium into the active materials can be determined from the complex nonlinear least squares (CNLS) fitting method, by fitting the impedance spectra to the equivalent circuit [39–41].

## References

1. Zhang Y, Shin HC, Dong J, Liu M (2004) Nanostructured  $\text{LiMn}_2\text{O}_4$  prepared by a glycine-nitrate process for lithium-ion batteries. *Solid State Ion* 171:25–31
2. Shin HC, Pyun SI (2001) Investigation of lithium transport through lithium cobalt dioxide thin film sputter-deposited by analysis of cyclic voltammogram. *Electrochim Acta* 46:2477–2485
3. Jung HR, Kim EJ, Park YJ, Shin HC (2011) Nickel–tin foam with nanostructured walls for rechargeable lithium battery. *J Power Sources* 196:5122–5127
4. Shin HC, Liu M (2005) Three-dimensional porous copper-tin alloy electrodes for rechargeable lithium batteries. *Adv Funct Mater* 15:582–586
5. Larcher D, Beaulieu LY, MacNeil DD, Dahn JR (2000) In situ X-ray study of the electrochemical reaction of Li with  $\eta\text{-Cu}_6\text{Sn}_5$ . *J Electrochem Soc* 147:1658–1662
6. Fransson L, Nordstrom E, Edstrom K, Haggstrom L, Vaughey JT, Thackeray MM (2002) Structural transformations in Lithiated  $\eta\text{-Cu}_6\text{Sn}_5$  electrodes probed by In situ Mössbauer spectroscopy and X-ray diffraction. *J Electrochem Soc* 149:A736–A742
7. Choi YM, Pyun SI, Moon SI, Hyung YE (1998) A study of the electrochemical lithium intercalation behavior of porous  $\text{LiNiO}_2$  electrodes prepared by solid-state reaction and sol–gel methods. *J Power Sources* 72:83–90
8. Weppner W, Huggins RA (1977) Determination of the kinetic parameters of mixed-conducting electrodes and application to the system  $\text{Li}_3\text{Sb}$ . *J Electrochem Soc* 124:1569–1578
9. Choi YM, Pyun SI, Bae JS, Moon SI (1995) Effects of lithium content on the electrochemical lithium intercalation reaction into  $\text{LiNiO}_2$  and  $\text{LiCoO}_2$  electrodes. *J Power Sources* 56:25–30
10. Bae JS, Pyun SI (1995) Electrochemical lithium intercalation reaction of anodic vanadium oxide film. *J Alloys Comp* 217:52–58
11. Carslaw HS, Jaeger JC (1959) *Conduction of heat in solids*. Clarendon, Oxford
12. Crank J (1975) *The mathematics of diffusion*. Clarendon, Oxford
13. Wen CJ, Boukamp BA, Huggins RA, Weppner W (1979) Thermodynamic and mass transport properties of “LiAl”. *J Electrochem Soc* 126:2258–2266
14. Shin HC, Pyun SI (1999) The kinetics of lithium transport through  $\text{Li}_{1-\delta}\text{CoO}_2$  by theoretical analysis of current transient. *Electrochim Acta* 45:489–501
15. Shin HC, Han JN, Pyun SI (1998) Fundamentals of current transient technique and their applications to interfacial electrochemistry. *J Corros Sci Soc Korea* 27:232–245

16. Striebel KA, Deng CZ, Wen SJ, Cairns EJ (1996) Electrochemical behavior of  $\text{LiMn}_2\text{O}_4$  and  $\text{LiCoO}_2$  thin films produced with pulsed laser deposition. *J Electrochem Soc* 143:1821–1827
17. Uchida T, Morikawa Y, Ikuta H, Wakihara M, Suzuki K (1996) Chemical diffusion coefficient of lithium in carbon fiber. *J Electrochem Soc* 143:2606–2610
18. Sato H, Takahashi D, Nishina T, Uchida I (1997) Electrochemical characterization of thin-film  $\text{LiCoO}_2$  electrodes in propylene carbonate solutions. *J Power Sources* 68:540–544
19. Zhang D, Popov BN, White RE (2000) Modeling lithium intercalation of a single spinel particle under potentiodynamic control. *J Electrochem Soc* 147:831–838
20. Choi YM, Pyun SI, Paulsen JM (1998) Lithium transport through porous  $\text{Li}_{1-\delta}\text{CoO}_2$  electrode: analysis of current transient. *Electrochim Acta* 44:623–632
21. Bae JS, Pyun SI (1996) Electrochemical lithium intercalation into and deintercalation from vanadium oxide electrode by using potentiostatic current transient technique. *Solid State Ionics* 90:251–260
22. Pyun SI, Choi YM (1997) Electrochemical lithium intercalation into and de-intercalation from porous  $\text{LiCoO}_2$  electrode by using potentiostatic current transient technique. *J Power Sources* 68:524–529
23. Pyun SI, Ryu YG (1998) Lithium transport through graphite electrodes that contain two stage phases. *J Power Sources* 70:34–39
24. Pyun SI, Yang TH (1998) Theoretical analysis of hydrogen transport through an electrode at the coexistence of two hydrogen-poor and -rich phases based upon the concept of hydrogen trapping. *J Electroanal Chem* 441:183–189
25. Kim DJ, Pyun SI (1998) Hydrogen transport through anodic  $\text{WO}_3$  films. *Electrochim Acta* 43:2341–2347
26. Isidorsson J, Strømme M, Gahlin R, Niklasson GA, Granqvist CG (1996) Ion transport in porous Sn oxide films: cyclic voltammograms interpreted in terms of a fractal dimension. *Solid State Commun* 99:109–111
27. Mattsson MS, Niklasson GA, Granqvist CG (1996) Fractal dimension of Li insertion electrodes studied by diffusion-controlled voltammetry and impedance spectroscopy. *Phys Rev B* 54:2968–2971
28. Shin HC, Pyun SI (1999) An investigation of the electrochemical intercalation of lithium into a  $\text{Li}_{1-\delta}\text{CoO}_2$  electrode based upon numerical analysis of potentiostatic current transients. *Electrochim Acta* 44:2235–2244
29. Funabiki A, Inaba M, Abe T, Ogumi Z (1999) Nucleation and phase-boundary movement upon stage transformation in lithium–graphite intercalation compounds. *Electrochim Acta* 45:865–871
30. Shin HC, Pyun SI, Kim SW, Lee MH (2001) Mechanisms of lithium transport through transition metal oxides studied by analysis of current transients. *Electrochim Acta* 46:897–906
31. Shin HC, Pyun SI (2003) Modern aspects of electrochemistry no. 36. In: Vayenas CG, Conway BE, White RE (eds) Chapter 5 Mechanisms of lithium transport through transition metal oxides and carbonaceous materials. Kluwer/Plenum, New York
32. Shin HC, Liu M, Sadanadan B, Rao AM (2002) Electrochemical insertion of lithium into multi-walled carbon nanotubes prepared by catalytic decomposition. *J Power Sources* 112:216–221
33. Bard AJ, Faulkner L (1980) *Electrochemical methods*. Wiley, New York
34. Aoki K, Tokuda K, Matsuda H (1983) Theory of linear sweep voltammetry with finite diffusion space. *J Electroanal Chem* 146:417–424
35. Ho C, Raistrick ID, Huggins RA (1980) Application of A-C techniques to the study of lithium diffusion in tungsten trioxide thin films. *J Electrochem Soc* 127:343–350
36. Cho HM, Choi WS, Go JY, Bae SE, Shin HC (2012) A study on time-dependent low temperature power performance of a lithium-ion battery. *J Power Sources* 198:273–280
37. Choi YM, Pyun SI (1997) Effects of intercalation-induced stress on lithium transport through porous  $\text{LiCoO}_2$  electrode. *Solid State Ionics* 99:173–183

38. Aurbach D, Levi MD, Levi E, Teller H, Markovsky B, Salitra G, Heider U, Heider L (1998) Common electroanalytical behavior of Li intercalation processes into graphite and transition metal oxides. *J Electrochem Soc* 145:3024–3034
39. Macdonald JR, Garber JA (1977) Analysis of impedance and admittance data for solids and liquids. *J Electrochem Soc* 124:1022–1030
40. Macdonald JR (1987) *Impedance spectroscopy*. Wiley, New York
41. Bae JS, Pyun SI (1994) An a.c. impedance study of LiI-Al<sub>2</sub>O<sub>3</sub> composite solid electrolyte. *J Mater Sci Lett* 13:573–576



<http://www.springer.com/978-3-642-29463-1>

Electrochemistry of Insertion Materials for Hydrogen  
and Lithium

Pyun, S.-I.; Shin, H.-C.; Lee, J.-W.; Go, J.-Y.

2012, X, 250 p., Hardcover

ISBN: 978-3-642-29463-1